

Unmasking Weyl Fermions using Extreme Magnetic Fields

B. J. Ramshaw,^{1,2} K. A. Modic,³ Arkady Shekhter,⁴ Yi Zhang,¹ Eun-Ah Kim,¹
Philip J. W. Moll,³ Maja Bachmann,³ M. K. Chan,² J. B. Betts,² F. Balakirev,²
A. Migliori,² N. J. Ghimire,^{5,2} E. D. Bauer,² F. Ronning,² and R. D. McDonald²

¹*Laboratory of Atomic and Solid State Physics,*

Cornell University, Ithaca, NY, 14853.

²*Los Alamos National Laboratory, Los Alamos, New Mexico, 87545.*

³*Max-Planck-Institute for Chemical Physics of Solids, Noethnitzer Strasse 40.*

⁴*National High Magnetic Field Laboratory, Tallahassee, Florida, 32310.*

⁵*Argonne National Laboratory, Argonne, Illinois, 60439.*

Weyl semimetals are a new class of materials that host an unusual type of massless particle predicted by quantum field theory—Weyl fermions. Unlike electrons in conventional metals, which come in ‘spin-up’ and ‘spin-down’ variants, Weyl fermions have chiral ‘left-handed’ and ‘right-handed’ variants. These exotic quasiparticles represent a new ingredient in the search for correlated states of electronic matter. A key difficulty has been that real materials also contain non-Weyl or ‘trivial’ electrons, and disentangling the experimental signatures of the Weyl fermions has proven challenging. Here we use magnetic fields up to 95 tesla to drive the Weyl semimetal TaAs far into its quantum limit (QL), where only the purely chiral 0th energy levels (Landau levels (LLs)) belonging to the Weyl fermions are occupied and where they can be studied in isolation. Up to 50 tesla we find the electrical resistivity to be nearly independent of magnetic field: unusual for a conventional metal in the QL but consistent with the chiral anomaly for Weyl fermions. Above 50 tesla we observe a two-order-of-magnitude increase in resistivity, indicating that a gap has opened in the chiral LLs and providing a bulk measure of the Weyl-node separation. Above 80 tesla we observe strong ultrasonic attenuation below 2 kelvin, suggesting a new mesoscopically-textured state of matter—reminiscent of the Coulomb-driven ‘microemulsion’ phases in two dimensions. These results show how high magnetic fields can be used to overcome material constraints and access a state composed purely of Weyl fermions, and point the way to inducing new correlated states of matter composed of these exotic quasiparticles.

The principle of emergence is beautifully demonstrated by the complex states of matter that arise in metals due to interactions. Starting with simple ingredients—electrons with a quadratic energy-momentum relationship and degenerate spin ‘up’ and ‘down’ states—otherwise conventional metals can become superconductors [1, 2], spontaneously break spatial symmetries [3], emerge with fractionalized charge [4], or even become insulating [5]. The recent prediction [6, 7] and discovery [8, 9] of Weyl semimetals brings a new ingredient to the table—Weyl fermions—that differ from conventional electrons in two key ways. First, they obey a linear or ‘massless’ energy-momentum relationship, analogous to electrons in graphene but in three

dimensions. Second, because of strong spin-orbit coupling and inversion symmetry breaking, spin ‘up’ and ‘down’ states are replaced by chiral ‘left’ and ‘right’-handed states (Figure 1a) [10]. Can interacting Weyl fermions form states of matter that are unique from those that arise in conventional metals? Predictions include chiral excitonic [11] and density wave states [12], topologically non-trivial superconductors [13, 14], and Tomonaga-Luttinger liquids [15], but no interacting states have been confirmed in Weyl semimetals to date. The multitude of different Weyl fermions and trivial quasiparticles that exist in real Weyl semimetals complicate matters by making it difficult to tell which effects are due to Weyl fermions and which effects can be ascribed to conventional semimetal physics [16].

In addition to the possibility of new correlated states, Weyl semimetals exhibit a number of unusual non-interacting properties due to the chiral anomaly. Chirality, or ‘handedness’, is a classically conserved quantity—the flows of left and right-handed quasiparticles (chiral currents) should be separately conserved. The correct quantum mechanical description of nature does not obey this symmetry, allowing for classically-forbidden phenomena such as the decay of a neutral pion into two photons [17, 18]. In the case of Weyl fermions it has been shown that parallel electric and magnetic fields can unbalance the number of left and right-handed Weyl fermions [10], leading to exotic transport [10, 19–21] and optical [22] properties. While this effect was originally predicted for a Weyl semimetal far in the QL [10], most experiments probing these effects have focused on relatively low magnetic fields [9, 23–25]. Again, interpretation of these results is hampered by the fact that there are multiple Weyl fermions and non-chiral quasiparticles all present at the Fermi energy.

Figure 1b shows the resistivity of the Weyl semimetal TaAs in magnetic fields up to 95 tesla. Immediately striking is the two-order-of-magnitude increase in resistance that onsets at 50 tesla for the current and field configuration $\vec{J} \parallel \vec{B} \parallel \hat{c}$ (note the logarithmic scale). In addition to its strong magnetic field dependence, ρ_{zz} is also strongly temperature dependent above 50 tesla. This is in contrast with the behaviour at intermediate fields (between 7.5 and 50 tesla), where ρ_{zz} decreases and then saturates, becoming roughly temperature and field independent. We identify the transport behaviour between 7.5 and 50 tesla as characteristic of the chiral anomaly

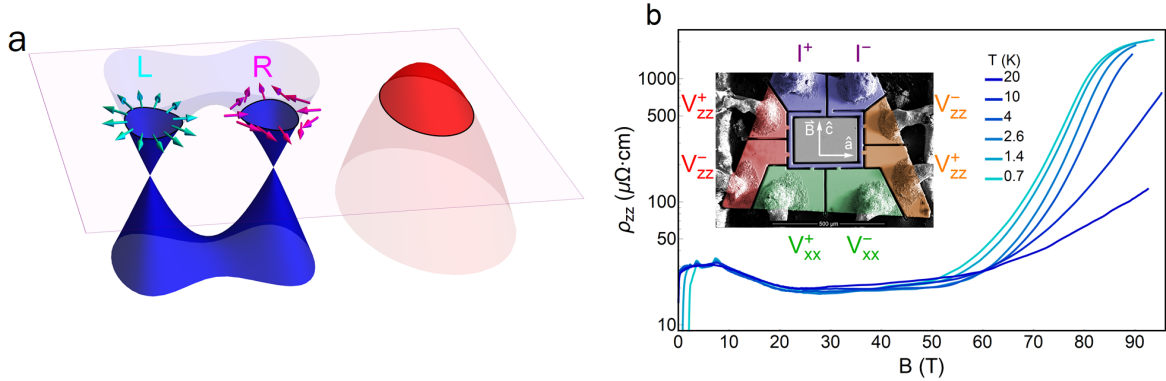


FIG. 1. **Weyl fermions and quantum limit transport in TaAs.** **a**, the Weyl semimetal TaAs contains three types of charge carriers: trivial holes (red), and two sets of electron-like Weyl fermions, designated W1 and W2, one of which is shown here in blue. The holes are of a single non-chiral carrier type, and contribute a non-Weyl background signature to experiments. The Weyl electrons are separated into distinct right and left-handed chiralities: arrows indicate the winding of the pseudospin around each Fermi surface. **b**, Resistivity of TaAs for $\vec{J} \parallel \vec{B} \parallel \hat{c}$ from 0.7 to 20 K. Quantum oscillations from the Weyl pockets are visible up to 7.5 tesla, followed by a decrease and then saturation of ρ_{zz} up to 50 tesla. Above 50 tesla there is a two order-of-magnitude increase in ρ_{zz} at low temperature, signifying the opening of a gap. The inset shows single-crystal TaAs microstructured using focused-ion-beam (FIB) lithography for both the ρ_{zz} and ρ_{xx} measurements.

in the QL for Weyl fermions, and the behaviour above 50 tesla as indicative of mixing between left and right handed Weyl fermions. There are two features in the data that we do not believe to be inherent to the bulk transport of TaAs: a superconducting transition at low field, originating in a ≈ 20 nm amorphous layer induced during sample preparation [26]; and the rollover of ρ_{zz} at high field, either due to the same amorphous layer or due to the intrinsic surface states of TaAs [9, 27, 28]. Neither effect impacts the conclusions of this paper (see SI).

We measure both $\vec{J} \parallel \vec{B} \parallel \hat{c} \rightarrow \rho_{zz}$ —and $\vec{J} \perp (\vec{B} \parallel \hat{c}) \rightarrow \rho_{xx}$ —to identify different regimes in the electronic structure of TaAs (Figure 2). TaAs contains three distinct types of quasiparticles: two electron-like Weyl Fermi surfaces (denoted W1 and W2 [9, 23, 25, 27, 29]), and hole-like Fermi surface with a ‘trivial’ spectrum [23, 29, 30]. Figure 2c highlights a key difference in

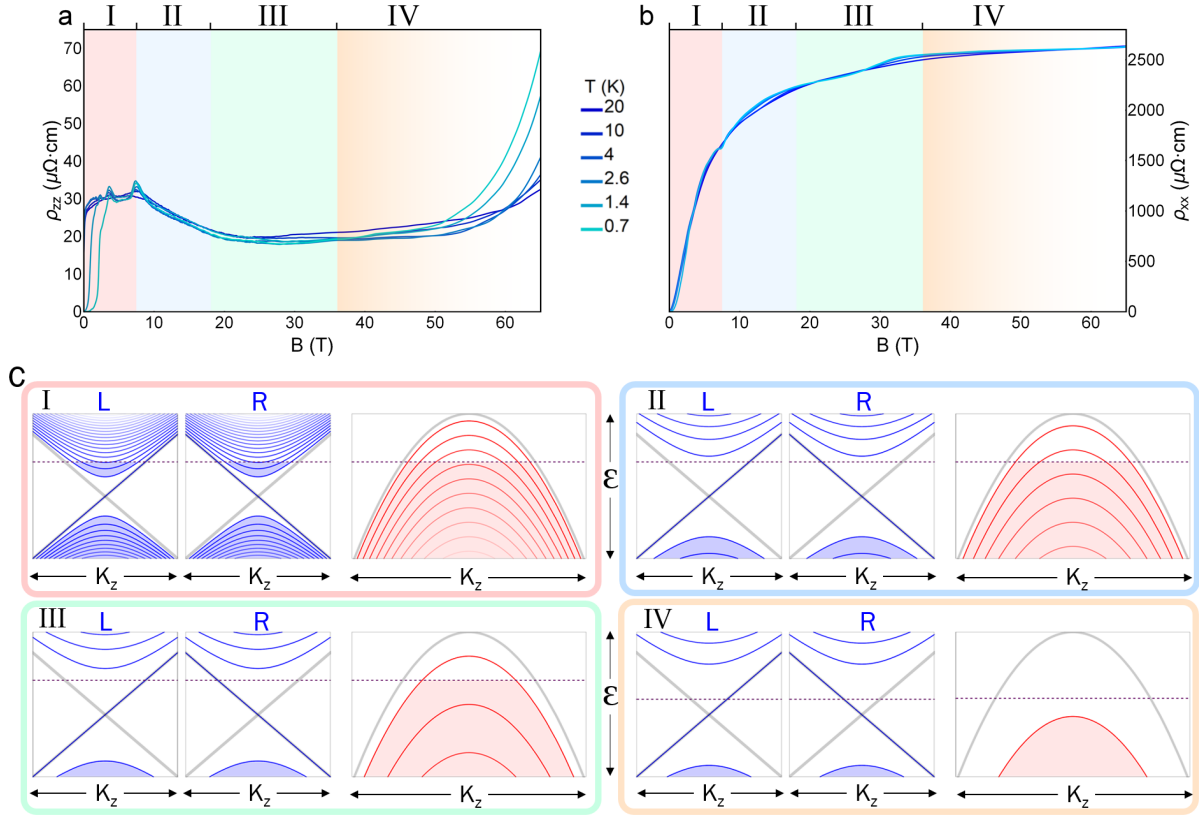


FIG. 2. **The four distinct regimes of Landau level occupancy in TaAs up to 65 tesla.** TaAs hosts two pairs of Weyl fermi surfaces (W1 and W2) with similar quantum limits for this field orientation; one pair of Weyl nodes is shown here along with the trivial hole surface. Resistivity of TaAs at temperatures between 0.7 K and 20 K, for $\vec{J} \parallel \vec{B} \parallel \hat{c}$ (a) and for $\vec{J} \perp (\vec{B} \parallel \hat{c})$ (b), from 0 to 65 tesla. c, Schematic of the Landau level (LL) structure and occupancy for the parabolic hole pockets (red lines) and Weyl electron pockets (blue lines). Grey curves are the $B = 0$ dispersions without LLs. Region I is from 0 to 7.5 tesla, where both hole and electron pockets exhibit quantum oscillations. Between 7.5 and 18 tesla (region II) the electron pockets are in the $n = 0$ LL, whereas the hole pocket is still in the $n = 1$ LL. Between 18 and 36 tesla (region III) the hole pocket is also in the $n = 0$ LL. At 36 tesla the last oscillation, corresponding to emptying the $n = 0$ LL of the hole pocket, can be seen in ρ_{xx} . Above 36 tesla (region IV) the only occupied states at the chemical potential are in the $n = 0$ LL of the Weyl electron pockets, and the chemical potential shifts to maintain overall carrier number ($n_e - n_h$). The faded region IV represents the mixing of the Weyl nodes above 50 tesla (Figure 3).

the Landau quantization between Weyl and trivial carriers: the energy of the $n = 0$ LL of Weyl carriers is field-independent and disperses linearly in k_z (momentum parallel to \vec{B}), whereas the energy of the $n = 0$ LL of trivial carriers is field-dependent and disperses quadratically in k_z . This leads to qualitatively different behaviour for the two carrier types in the QL, when only the $n = 0$ LL is occupied [31]. As the magnetic field is increased TaAs passes through four distinct LL regimes, described in detail in the caption to Figure 2. The fact that the trivial hole carriers can be completely depopulated with field is a result of the field-independence of the $n = 0$ LL of the Weyl carriers. The field at which this depopulation occurs—36 tesla—agrees quantitatively with previous Fermi surface geometry measurements [29].

Above 36 tesla the chiral $n = 0$ LLs of the Weyl fermions can be studied without the complicating influence of trivial holes, and without the $n > 0$ LLs for which chirality is not well-defined [32]. Each of the two 0th LLs of the Weyl fermions contains carriers propagating along a single direction—parallel to \vec{B} for one chirality (‘up movers’), and anti-parallel for the other (‘down movers’). Applying an electric field (driving current) parallel to \vec{B} produces an imbalance in the number of up versus down movers, resulting in an imbalance of left and right-handed carriers—a chiral anomaly. The difference in number of up versus down movers produces a chiral current, effectively increasing the conductivity as the electric and magnetic fields transfer charge from one Weyl node to the other [10, 19]. The experimental signature of this phenomenon at low fields—negative magnetoresistance—has been controversial due to the presence of experimental artifacts [32–34] and contributions from the trivial hole pocket. We find that using focused-ion-beam lithography (FIB) to reduce current-jetting can suppress or even eliminate the very low field negative magnetoresistance that has been reported for TaAs [7, 8] (see S.I.), in line with an earlier study of current-jetting [34]. We do observe negative magnetoresistance from 7.5 to 25 tesla which may be related to the chiral anomaly, although not all samples show this to the same degree and this effect may depend sensitively on sample alignment (see S.I.). Our focus is not on the low-field regime but instead on the QL where the behaviour of the chiral anomaly should be qualitatively distinct [20].

Deep in the QL, where transport along the z direction is determined by the $n = 0$ LL of the

Weyl fermions alone, the conductivity has the form

$$\sigma_{zz} = N_W \frac{e^2 v_F}{4\pi\hbar l_B^2} \tau_{inter}(B), \quad (1)$$

where N_W is the number of Weyl points in the Brillouin zone, v_F is the Fermi velocity, $l_B = \sqrt{\hbar/eB}$ is the magnetic length, and $\tau_{inter}(B)$ is the field-dependent inter-nodal scattering time [10, 20]. As shown below, the W1 Weyl nodes are most likely gapped in this field range (we use the notation of Arnold et al. [29] for W1 and W2, opposite that of Lv et al. [27]). We therefore evaluate Equation 1 for the eight W2 Weyl nodes, using v_F determined by the quantum oscillations (see S.I.). At 27 tesla, where σ_{zz} is maximum, we calculate $\tau_{inter} = 6$ ps. This is approximately 10 times longer than the *intra*-nodal scattering rate that we calculate from the Dingle factor of the quantum oscillations (see S.I.), confirming that the chiral 0th LLs carry current with a reduced scattering time in the QL due to their physical separation and distinct chiralities.

As the magnetic field is increased TaAs shows relatively constant resistivity in the QL before 50 tesla (Figure 1b), requiring that the scattering rate $1/\tau$ increases roughly in proportion to B to cancel the factor of l_B^2 in Equation 1. Indeed, $1/\tau \propto B$, and the resulting field-independent conductivity, was predicted for the QL of Weyl semimetals assuming short-range impurity scattering, suggesting that this is the dominant scattering mechanism between the Weyl nodes in TaAs [20]. As pointed out by Spivak and Andreev [20], short-range impurity scattering in the ultra-quantum limit of *conventional* semimetals leads to longitudinal magnetoresistance that increases strongly with magnetic field [35, 36]. Thus our observation of relatively constant ρ_{zz} up to 7 times the QL is a unique property of Weyl fermions.

Having established the QL transport properties of TaAs at intermediate fields we turn to higher fields where ρ_{zz} increases rapidly above 50 tesla (Figure 1b). While the 0th LLs of the Weyl nodes should naively remain metallic deep in the QL, the two-order-of-magnitude increase in ρ_{zz} suggests the formation of a gap. Weyl nodes are topologically stable to small perturbations [16], but this can be overcome by strong magnetic fields which mix the left and right-handed $n = 0$ LLs (Figure 3a). If the chemical potential falls within the gap then thermal activation is required to promote charge carriers to the empty LL, resulting in a strong temperature

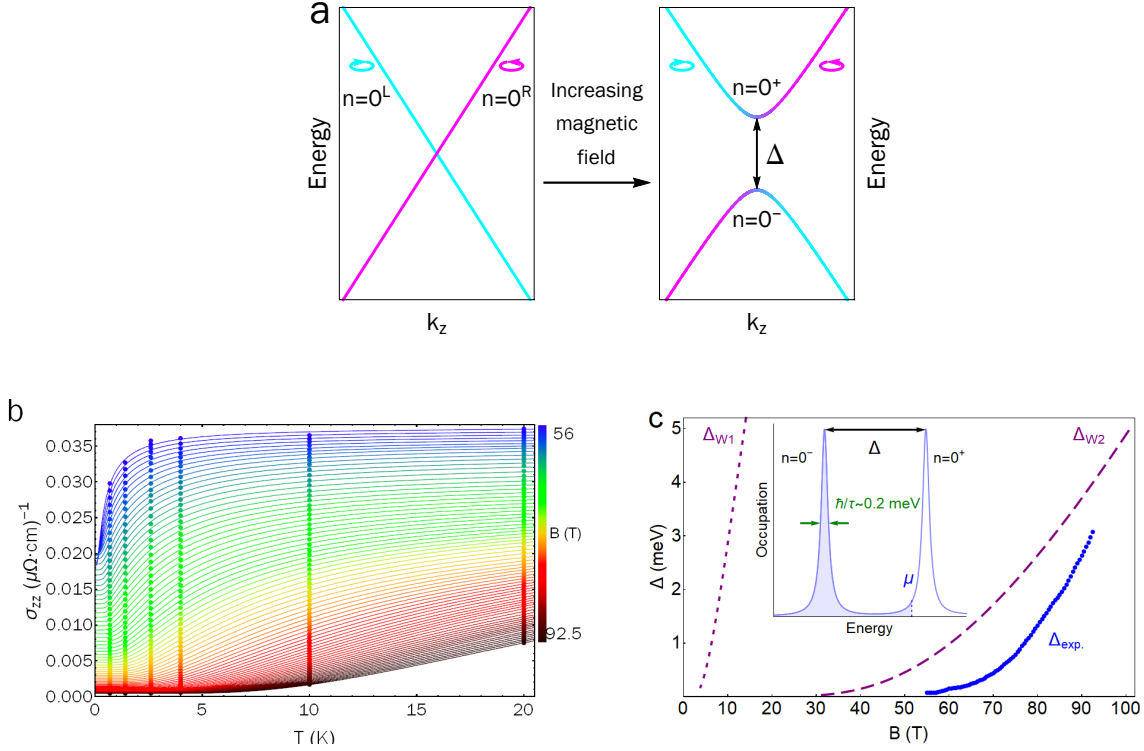


FIG. 3. Mixing of left and right-handed Landau levels in a magnetic field. The left and right-handed Weyl nodes are separated in the k_x - k_y plane in TaAs (Figure 1a) but are degenerate along k_z . At low magnetic fields the left and right-handed $n = 0$ LLs can be considered independent (a). As the magnetic field is increased, and the magnetic length approaches the inverse momentum-space separation of the nodes, the two LLs hybridize and a gap Δ opens that increases with field. We extract this gap by fitting the conductivity to $\sigma_{zz} = \sigma_0 + \sigma_1 e^{-\frac{\Delta}{k_B T}}$ from 56 to 92.5 tesla (b, points are data and solid lines are fits at different values of the magnetic field), with Δ show in panel c. We find that the W1 nodes gap at low field due to their close momentum-space proximity [7, 23, 25, 27], whereas the much larger separation of the W2 nodes means that their gap opens at higher field (b). The ≈ 0.5 meV offset between our calculated and measured gaps may be due to the ≈ 0.2 meV LL broadening due to finite quasiparticle lifetime (inset).

dependence for ρ_{zz} . As pointed out previously [37–39] a gap in the 0^{th} LLs should be observable when the inverse magnetic length $1/l_B = 1/\sqrt{(\hbar/eB)}$ —which controls the momentum-space extent of 0^{th} LL wavefunctions—becomes small compared to the momentum-space separation

of the Weyl nodes. This mechanism implies that the left and right handed chiral quasiparticles lose their distinction when their wavefunctions overlap, allowing for increased scattering between them and for the formation of a gap. It was shown by Chan and Lee [38] that band-structure estimates of the Weyl node separation produce a gap that onsets at a field much lower than what we observe. If this were to happen then there would be no experimental regime where the QL of the Weyl fermions could be studied. Instead we find a broad region in the QL where the gap remains exponentially small. The high sensitivity of the Weyl node separation to small shifts in the band structure means that transport measurements of the gap stand to produce the most accurate measure of Weyl node separation in the bulk.

To quantify this picture we extract the experimental gap by fitting the temperature-dependent conductivity at different values of the magnetic field where the gap opens above 56 tesla (Figure 3b). The data are well-described by the model $\sigma_{zz} = \sigma_0 + \sigma_1 e^{-\frac{\Delta}{k_B T}}$, where σ_0 is a field-dependent background, σ_1 is the conductivity from the 0th LLs, and Δ is the gap (plotted as Δ_{exp} in Figure 3c). This model assumes that the gap dominates the field-dependence of the transport and we keep the scattering rate fixed as function of field for simplicity. To relate this gap to the electronic structure of the Weyl nodes we developed a complete tight binding model of TaAs in a magnetic field, including all 24 Weyl nodes and Zeeman coupling (see S.I for a full description of the tight binding model and LL calculations). Fixing v_F to the experimentally determined value we find that $\delta k = 0.15\pi/a$ gives the correct slope of Δ versus B at high field. The slope of Δ versus B is a strong function of δk , and therefore provides a bulk-sensitive measurement of the Weyl node separation. Our extracted value of δk also fits the range of W2 node separation estimated by photoemission measurements (between $0.12\pi/a$ and $0.15\pi/a$) [9, 27]. The W1 nodes are estimated to be separated by at most $\delta k = 0.04\pi/a$, and are therefore gaped at much lower field (Figure 3c).

It should be noted that perfect electron-hole compensation is required for the chemical potential to lie in the gap at high fields: any excess of electrons (holes) will pin the chemical potential in the $n = 0^-$ ($n = 0^+$) LL to maintain the net carrier concentration. Hall effect measurements indicate that compensation in TaAs may not be perfect, with an estimated $2 \times 10^{17} \text{ cm}^{-3}$ to

$5 \times 10^{18} \text{ cm}^{-3}$ excess electrons [28, 29] that naively should remain metallic at high fields. In reality once the magnetic length is short enough that the left and right nodes overlap scattering will increase greatly and eventually localize any residual carriers. The estimated excess electron density in TaAs is $\approx 10^{12}$ carriers per cm^2 —within the range of a metal-insulator transition [40, 41]. This may account for the background conductivity σ_0 that we observe to decrease with increasing field (see S.I.). Note that we do not observe a similar increase in ρ_{xx} above 50 tesla: the in-plane conductivity has an 80 meV (1000 kelvin) cyclotron gap at 50 tesla, and in-plane transport in this regime is dominated by impurity-assisted hopping between adjacent $n = 0$ LLs in real space [36]. Thus ρ_{xx} should be weakly temperature dependent for $\vec{B} \parallel \hat{c}$, consistent with what we observe experimentally.

At 80 tesla, deep in the gapped state, we observe a small decrease in ρ_{xx} at the lowest temperatures (Figure 4a)—possibly indicative of a phase transition. To investigate this possibility further we measured the sound velocity (v_{zz}) of TaAs using pulse echo ultrasound up to 95 tesla, providing a thermodynamic probe at the highest fields. Below 2.5 K and above 80 tesla we observe an increase in sound velocity accompanied by a strong increase in ultrasonic attenuation (Figure 4b and c). The onset of these ultrasonic features coincides with the sharp decrease in ρ_{xx} , and we take all three phenomena as evidence for a field-induced phase transition. Our numerical solutions of the tight binding model predict no further transitions as a function of magnetic field once the gap opens along k_z , suggesting that this transition at 80 tesla is driven by interactions.

There is precedent for an interaction-driven phase transition deep in the quantum limit of a semimetal. Graphite, whose quantum limit is 7.5 tesla, undergoes a rich series of transitions above 30 tesla. These transitions are generally ascribed to excitonic or Peirels-type density-wave formation along the magnetic field direction [42–44]. This mechanism seems unlikely to occur in TaAs given that a gap has already opened along k_z at 50 tesla. In the limit where the ultrasonic wavelength is much longer than the quasiparticle mean free path, attenuation is proportional to conductivity [45]. The fact that we observe attenuation to increase while σ_{zz} *decreases* suggests that something other than conventional electronic attenuation is occurring

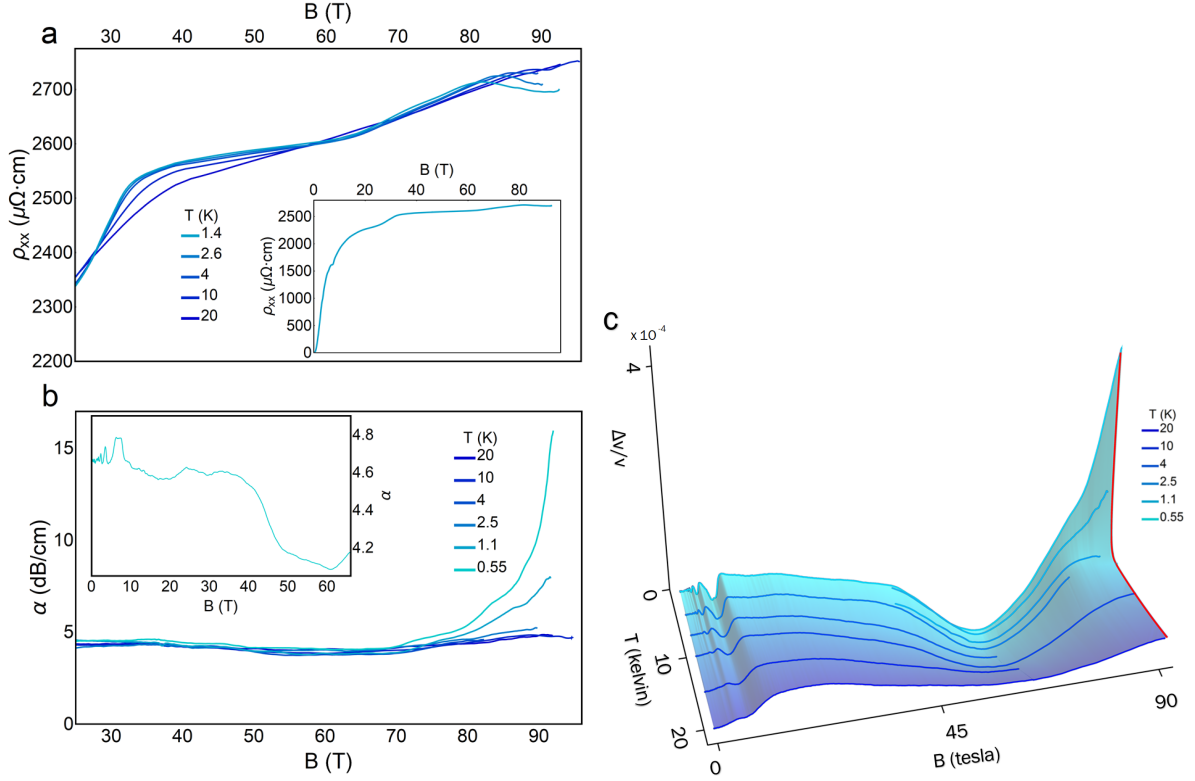


FIG. 4. **Phase transition deep in the quantum limit of TaAs.** **a**, Resistivity for $\vec{J} \perp (\vec{B} \parallel \hat{c})$, showing a kink near 80 tesla at low temperature. **b**, The ultrasonic attenuation at 315 MHz for $\vec{k} \parallel \vec{B} \parallel \hat{c}$, where \vec{k} is the propagation wavevector of the longitudinal (compressional) sound, and with data from 0 to 65 tesla shown in the inset. **c**, Change in the speed of sound for the same configuration as the attenuation shown in **b**. Data from two different experiments—one from 0 to 65 tesla and one from 45 to 95 tesla—are combined in this plot. Above 2.5 K the sound velocity flattens out above 80 tesla and the attenuation is only weakly field dependent. Below 2.5 K, however, both the sound velocity and the ultrasonic attenuation increase rapidly with field. The red line is an interpolation of the data, highlighting the abruptness of the transition as a function of temperature.

above 80 T in TaAs. The enhanced attenuation could come from the interaction between ultrasound and order-parameter fluctuations, as it does in graphite where it peaks near each phase transition [46]. The unbounded growth in attenuation we observe suggests that either we have

not yet reached the attenuation peak, or that a different attenuation mechanism is at work.

To speculate on the microscopic origin of the high-field phase it is helpful to consider which degree of freedom remains after the gap opens along k_z . The in-plane cyclotron orbits of the quasiparticles shrink in size with increasing magnetic field, resulting in a large real-space degeneracy of the $n = 0$ LLs (or equivalently momentum-space overlap of the quasiparticle wavefunctions). This increases the Coulomb repulsion between quasiparticles as $E_C \propto e^2/l_B$, ultimately leading to Wigner crystallization. Before this transition occurs, however, there are intermediate ‘mixed’ or ‘microemulsion’ phases with spatially phase-separated regions of Fermi liquid and bubbles of crystallized electrons [47]. Disorder pins these structures in real-space, resulting in a mesoscopically inhomogeneous system. This texture, with a length-scale comparable to the ultrasonic wavelength, is known to scatter ultrasound. Clearly this phase needs to be explored further before it can be identified: the frequency dependence of the attenuation would yield the length scale of the phase separation [48] or the frequency-dependence of the order parameter fluctuations [49]; the collective sliding motion of crystallized electrons can be revealed by nonlinear current-voltage measurements [50].

The ideal Weyl semimetal contains only one pair of Weyl nodes, with large momentum space separation to make them robust against perturbations. Reality is more interesting: the W2 Weyl nodes in TaAs have a large separation compared to other materials [7], but there are 12 pairs of nodes in total plus the trivial hole pockets. Using magnetic fields to drive Weyl semimetals into their QL provides a clear path forward for studying ‘pure’ Weyl physics, taking advantage of the fact that the 0th LLs are field-independent. This greatly broadens the number of potential systems where Weyl fermions can be accessed: as long as the magnetic field is strong enough the chemical potential will always move to the chiral 0th Weyl LLs in the quantum limit, even if the zero-field Fermi surface encompasses both nodes. Given that magnetic fields also increase the Coulomb interaction between quasiparticles (which can be particularly weak in semimetals due to the high Fermi velocities), the QL is also a promising regime for finding new states of

matter formed from Weyl fermions.

- [1] H Kamerlingh Onnes. The superconductivity of mercury. *Comm. Phys. Lab. Univ. Leiden*, 122: 124, 1911.
- [2] J George Bednorz and K Alex Müller. Possible hightc superconductivity in the ba- la- cu- o system. *Zeitschrift für Physik B Condensed Matter*, 64(2):189–193, 1986.
- [3] SA Kivelson, E Fradkin, VJ Emery, et al. Electronic liquid-crystal phases of a doped mott insulator. *Nature*, 393(6685):550–553, 1998.
- [4] D. C. Tsui, H. L. Stormer, and A. C. Gossard. Two-dimensional magnetotransport in the extreme quantum limit. *Phys. Rev. Lett.*, 48:1559–1562, May 1982. doi:10.1103/PhysRevLett.48.1559. URL <http://link.aps.org/doi/10.1103/PhysRevLett.48.1559>.
- [5] NF Mott. Metal-insulator transition. *Reviews of Modern Physics*, 40(4):677, 1968.
- [6] Xiangang Wan, Ari M. Turner, Ashvin Vishwanath, and Sergey Y. Savrasov. Topological semimetal and fermi-arc surface states in the electronic structure of pyrochlore iridates. *Phys. Rev. B*, 83: 205101, May 2011. doi:10.1103/PhysRevB.83.205101. URL <https://link.aps.org/doi/10.1103/PhysRevB.83.205101>.
- [7] Hongming Weng, Chen Fang, Zhong Fang, B. Andrei Bernevig, and Xi Dai. Weyl semimetal phase in noncentrosymmetric transition-metal monophosphides. *Phys. Rev. X*, 5:011029, Mar 2015. doi:10.1103/PhysRevX.5.011029. URL <https://link.aps.org/doi/10.1103/PhysRevX.5.011029>.
- [8] Su-Yang Xu, Ilya Belopolski, Nasser Alidoust, Madhab Neupane, Guang Bian, Chenglong Zhang, Raman Sankar, Guoqing Chang, Zhujun Yuan, Chi-Cheng Lee, Shin-Ming Huang, Hao Zheng, Jie Ma, Daniel S. Sanchez, BaoKai Wang, Arun Bansil, Fangcheng Chou, Pavel P. Shibayev, Hsin Lin, Shuang Jia, and M. Zahid Hasan. Discovery of a weyl fermion semimetal and topological fermi arcs. *Science*, 349(6248):613–617, 2015.
- [9] B. Q. Lv, H. M. Weng, B. B. Fu, X. P. Wang, H. Miao, J. Ma, P. Richard, X. C. Huang, L. X. Zhao,

- G. F. Chen, Z. Fang, X. Dai, T. Qian, and H. Ding. Experimental discovery of weyl semimetal taas. *Phys. Rev. X*, 5:031013, Jul 2015. doi:10.1103/PhysRevX.5.031013. URL <http://link.aps.org/doi/10.1103/PhysRevX.5.031013>.
- [10] Holger Bech Nielsen and Masao Ninomiya. The adler-bell-jackiw anomaly and weyl fermions in a crystal. *Physics Letters B*, 130(6):389–396, 1983.
- [11] Huazhou Wei, Sung-Po Chao, and Vivek Aji. Excitonic phases from weyl semimetals. *Phys. Rev. Lett.*, 109:196403, Nov 2012. doi:10.1103/PhysRevLett.109.196403. URL <https://link.aps.org/doi/10.1103/PhysRevLett.109.196403>.
- [12] Xiao-Tian Zhang and Ryuichi Shindou. Transport properties of density wave phases in three-dimensional metals and semimetals under high magnetic field. *Physical Review B*, 95(20):205108, 2017.
- [13] Gil Young Cho, Jens H. Bardarson, Yuan-Ming Lu, and Joel E. Moore. Superconductivity of doped weyl semimetals: Finite-momentum pairing and electronic analog of the ${}^3\text{he-a}$ phase. *Phys. Rev. B*, 86:214514, Dec 2012. doi:10.1103/PhysRevB.86.214514. URL <https://link.aps.org/doi/10.1103/PhysRevB.86.214514>.
- [14] Tobias Meng and Leon Balents. Weyl superconductors. *Phys. Rev. B*, 86:054504, Aug 2012. doi:10.1103/PhysRevB.86.054504. URL <https://link.aps.org/doi/10.1103/PhysRevB.86.054504>.
- [15] Xiao-Xiao Zhang and Naoto Nagaosa. Tomonaga-luttinger liquid and localization in weyl semimetals. *Phys. Rev. B*, 95:205143, May 2017. doi:10.1103/PhysRevB.95.205143. URL <https://link.aps.org/doi/10.1103/PhysRevB.95.205143>.
- [16] NP Armitage, EJ Mele, and Ashvin Vishwanath. Weyl and dirac semimetals in three dimensional solids. *arXiv preprint arXiv:1705.01111*, 2017.
- [17] Stephen L. Adler. Axial-vector vertex in spinor electrodynamics. *Phys. Rev.*, 177:2426–2438, Jan 1969. doi:10.1103/PhysRev.177.2426. URL <https://link.aps.org/doi/10.1103/PhysRev.177.2426>.
- [18] John S Bell and Roman Jackiw. A PCAC puzzle: $\pi^0 \gamma\gamma$ in the σ -model. *Il Nuovo Cimento A (1965-1970)*, 60(1):47–61, 1969.

- [19] D. T. Son and B. Z. Spivak. Chiral anomaly and classical negative magnetoresistance of weyl metals. *Phys. Rev. B*, 88:104412, Sep 2013. doi:10.1103/PhysRevB.88.104412. URL <https://link.aps.org/doi/10.1103/PhysRevB.88.104412>.
- [20] B. Z. Spivak and A. V. Andreev. Magnetotransport phenomena related to the chiral anomaly in weyl semimetals. *Phys. Rev. B*, 93:085107, Feb 2016. doi:10.1103/PhysRevB.93.085107. URL <http://link.aps.org/doi/10.1103/PhysRevB.93.085107>.
- [21] Andrew Lucas, Richard A Davison, and Subir Sachdev. Hydrodynamic theory of thermoelectric transport and negative magnetoresistance in weyl semimetals. *Proceedings of the National Academy of Sciences*, page 201608881, 2016.
- [22] Pavan Hosur and Xiao-Liang Qi. Tunable circular dichroism due to the chiral anomaly in weyl semimetals. *Physical Review B*, 91(8):081106, 2015.
- [23] Xiaochun Huang, Lingxiao Zhao, Yujia Long, Peipei Wang, Dong Chen, Zhanhai Yang, Hui Liang, Mianqi Xue, Hongming Weng, Zhong Fang, Xi Dai, and Genfu Chen. Observation of the chiral-anomaly-induced negative magnetoresistance in 3d weyl semimetal taas. *Phys. Rev. X*, 5:031023, Aug 2015. doi:10.1103/PhysRevX.5.031023. URL <http://link.aps.org/doi/10.1103/PhysRevX.5.031023>.
- [24] Johannes Gooth, Anna Corinna Niemann, Tobias Meng, Adolfo G Grushin, Karl Landsteiner, Bernd Gotsmann, Fabian Menges, Marcus Schmidt, Chandra Shekhar, Vicky Sueß, et al. Experimental signatures of the mixed axial-gravitational anomaly in the weyl semimetal nbp. *arXiv preprint arXiv:1703.10682*, 2017.
- [25] Qiong Ma, Su-Yang Xu, Ching-Kit Chan, Cheng-Long Zhang, Guoqing Chang, Yuxuan Lin, Weiwei Xie, Tomás Palacios, Hsin Lin, Shuang Jia, et al. Direct optical detection of weyl fermion chirality in a topological semimetal. *arXiv preprint arXiv:1705.00590*, 2017.
- [26] Maja D. Bachmann, Nityan Nair, Felix Flicker, Roni Ilan, Tobias Meng, Nirmal J. Ghimire, Eric D. Bauer, Filip Ronning, James G. Analytis, and Philip J. W. Moll. Inducing superconductivity in weyl semi-metal microstructures by selective ion sputtering. *arxiv.org*, 2017.
- [27] BQ Lv, N Xu, HM Weng, JZ Ma, P Richard, XC Huang, LX Zhao, GF Chen, CE Matt, F Bisti, et al. Observation of weyl nodes in taas. *Nature Physics*, 11:724–727, 2015.

- [28] Cheng-Long Zhang, Zhujun Yuan, Qing-Dong Jiang, Bingbing Tong, Chi Zhang, X. C. Xie, and Shuang Jia. Electron scattering in tantalum monoarsenide. *Phys. Rev. B*, 95:085202, Feb 2017. doi:10.1103/PhysRevB.95.085202. URL <https://link.aps.org/doi/10.1103/PhysRevB.95.085202>.
- [29] F. Arnold, M. Naumann, S.-C. Wu, Y. Sun, M. Schmidt, H. Borrmann, C. Felser, B. Yan, and E. Hassinger. Chiral weyl pockets and fermi surface topology of the weyl semimetal taas. *Phys. Rev. Lett.*, 117:146401, Sep 2016. doi:10.1103/PhysRevLett.117.146401. URL <https://link.aps.org/doi/10.1103/PhysRevLett.117.146401>.
- [30] Cheng-Long Zhang, Su-Yang Xu, Ilya Belopolski, Zhujun Yuan, Ziquan Lin, Bingbing Tong, Guang Bian, Nasser Alidoust, Chi-Cheng Lee, Shin-Ming Huang, Tay-Rong Chang, Guoqing Chang, Chuang-Han Hsu, Horng-Tay Jeng, Madhab Neupane, Daniel S. Sanchez, Hao Zheng, Junfeng Wang, Hsin Lin, Chi Zhang, Hai-Zhou Lu, Shun-Qing Shen, Titus Neupert, M. Zahid Hasan, and Shuang Jia. Signatures of the adler-bell-jackiw chiral anomaly in a weyl fermion semimetal. *Nature Communications*, 7, Feb 2016. ISSN 2041-1723. doi:10.1038/ncomms10735.
- [31] Philip J. W. Moll, Andrew C. Potter, Nityan L. Nair, B. J. Ramshaw, K. A. Modic, Scott Riggs, Bin Zeng, Nirmal J. Ghimire, Eric D. Bauer, Robert Kealhofer, Filip Ronning, and James G. Analytis. Magnetic torque anomaly in the quantum limit of weyl semimetals. *Nature Communications*, 7, Aug 2016. ISSN 2041-1723. doi:10.1038/ncomms12492.
- [32] Frank Arnold, Chandra Shekhar, Shu-Chun Wu, Yan Sun, Ricardo Donizeth dos Reis, Nitesh Kumar, Marcel Naumann, Mukkattu O Ajeesh, Marcus Schmidt, Adolfo G Grushin, et al. Negative magnetoresistance without well-defined chirality in the weyl semimetal tap. *Nature communications*, 7, 2016.
- [33] Alfred Brian Pippard. *Magnetoresistance in metals*, volume 2. Cambridge University Press, 1989.
- [34] R. D. dos Reis, M. O. Ajeesh, N. Kumar, F. Arnold, C. Shekhar, M. Naumann, M. Schmidt, M. Nicklas, and E. Hassinger. On the search for the chiral anomaly in weyl semimetals: the negative longitudinal magnetoresistance. *New Journal of Physics*, 18, Aug 11 2016. ISSN 1367-2630. doi:10.1088/1367-2630/18/8/085006.
- [35] PN Argyres and EN Adams. Longitudinal magnetoresistance in the quantum limit. *Physical Re-*

- view, 104(4):900, 1956.
- [36] Sergei Stanislavovich Murzin. Electron transport in the extreme quantum limit in applied magnetic field. *Physics-Uspekhi*, 43(4):349–364, 2000.
- [37] Pilkwang Kim, Ji Hoon Ryoo, and Cheol-Hwan Park. The chiral anomaly in weyl semimetals is not robust. *arXiv preprint arXiv:1707.01103*, 2017.
- [38] Ching-Kit Chan and Patrick A Lee. Anticrossing of chiral landau levels in dirac and weyl semimetals. *arXiv preprint arXiv:1708.06472*, 2017.
- [39] Cheng-Long Zhang, Su-Yang Xu, CM Wang, Ziquan Lin, ZZ Du, Cheng Guo, Chi-Cheng Lee, Hong Lu, Yiyang Feng, Shin-Ming Huang, et al. Magnetic-tunnelling-induced weyl node annihilation in tap. *Nature Physics*, 13(10):979–986, 2017.
- [40] Dragana Popović, AB Fowler, and S Washburn. Metal-insulator transition in two dimensions: Effects of disorder and magnetic field. *Physical review letters*, 79(8):1543, 1997.
- [41] Sergey V Kravchenko, GV Kravchenko, JE Furneaux, Vladimir M Pudalov, and M dIorio. Possible metal-insulator transition at $b=0$ in two dimensions. *Physical Review B*, 50(11):8039, 1994.
- [42] S Tanuma, R Inada, A Furukawa, O Takahashi, Y Iye, Y Onuki, S Chikazumi, and N Miura. Physics in high magnetic fields. *Springer Series in Solid State Sciences*, 1981.
- [43] Benoît Fauqué, David LeBoeuf, Baptiste Vignolle, Marc Nardone, Cyril Proust, and Kamran Behnia. Two phase transitions induced by a magnetic field in graphite. *Phys. Rev. Lett.*, 110:266601, Jun 2013. doi:10.1103/PhysRevLett.110.266601. URL <http://link.aps.org/doi/10.1103/PhysRevLett.110.266601>.
- [44] Z Zhu, RD McDonald, A Shekhter, B.J. Ramshaw, KA Modic, FF Balakirev, and N Harrison. Tunable excitonic insulator in quantum limit graphite. *arXiv preprint arXiv:1508.03645*, 2015.
- [45] AB Pippard. Ultrasonic attenuation in metals. *Philosophical Magazine*, 46(381):1104–1114, 1955. ISSN 0031-8086.
- [46] D LeBoeuf, CW Rischau, G Seyfarth, R Küchler, M Berben, S Wiedmann, W Tabis, M Frchet, K Behnia, and B Fauqué. Thermodynamic signatures of the field-induced states of graphite. *arXiv preprint arXiv:1705.07056*, 2017.
- [47] Boris Spivak and Steven A Kivelson. Transport in two dimensional electronic micro-emulsions.

- Annals of Physics*, 321(9):2071–2115, 2006.
- [48] M. A. Paalanen, R. L. Willett, P. B. Littlewood, R. R. Ruel, K. W. West, L. N. Pfeiffer, and D. J. Bishop. rf conductivity of a two-dimensional electron system at small landau-level filling factors. *Phys. Rev. B*, 45:11342–11345, May 1992. doi:10.1103/PhysRevB.45.11342. URL <https://link.aps.org/doi/10.1103/PhysRevB.45.11342>.
- [49] Arkady Shekhter, BJ Ramshaw, Ruixing Liang, WN Hardy, DA Bonn, Fedor F Balakirev, Ross D McDonald, Jon B Betts, Scott C Riggs, and Albert Migliori. Bounding the pseudogap with a line of phase transitions in $\text{YBa}_2\text{Cu}_3\text{O}_{6+x}$ [dgr]. *Nature*, 498(7452):75–77, 2013.
- [50] Stuart B. Field, D. H. Reich, B. S. Shivaram, T. F. Rosenbaum, D. A. Nelson, and P. B. Littlewood. Evidence for depinning of a wigner crystal in hg-cd-te. *Phys. Rev. B*, 33:5082–5085, Apr 1986. doi:10.1103/PhysRevB.33.5082. URL <https://link.aps.org/doi/10.1103/PhysRevB.33.5082>.
- [51] D. Shoenberg. *Magnetic oscillations in metals*. Cambridge monographs on physics. Cambridge University Press, 1984. ISBN 9780521224802.
- [52] BJ Ramshaw, Baptiste Vignolle, James Day, Ruixing Liang, WN Hardy, Cyril Proust, and DA Bonn. Angle dependence of quantum oscillations in $\text{YBa}_2\text{Cu}_3\text{O}_6$. 59 shows free-spin behaviour of quasiparticles. *Nature Physics*, 7(3):234–238, 2011.
- [53] K Brugger. Pure modes for elastic waves in crystals. *Journal of Applied Physics*, 36(3):759–768, 1965.
- [54] A Suslov, Bimal K Sarma, JB Ketterson, F Balakirev, A Migliori, and A Lacerda. Ultrasonic instrumentation for measurements in high magnetic fields. ii. pulsed magnetic fields. *Review of scientific instruments*, 77(3):035105, 2006.
- [55] Ari M. Turner, Yi Zhang, Roger S. K. Mong, and Ashvin Vishwanath. Quantized response and topology of magnetic insulators with inversion symmetry. *Phys. Rev. B*, 85:165120, Apr 2012. doi:10.1103/PhysRevB.85.165120. URL <https://link.aps.org/doi/10.1103/PhysRevB.85.165120>.

ACKNOWLEDGMENTS

This work was performed at the National High Magnetic Field Laboratory, which is supported by National Science Foundation Cooperative Agreement No. DMR-1157490 and the State of Florida. E.D.B, F.R., and R.D.M. acknowledge funding from the LANL LDRD DR20160085 ‘Topology and Strong Correlations’. B.J.R. acknowledges funding from LANL LDRD 20160616ECR ‘New States of Matter in Weyl Semimetals’. M.K.C. acknowledges funding from the U.S. Department of Energy Office of Basic Energy Sciences Science at 100 T program. YZ was supported in part by NSF DMR-1308089 and EAK was supported in part by National Science Foundation (Platform for the Accelerated Realization, Analysis, and Discovery of Interface Materials (PARADIM)) under Cooperative Agreement No. DMR-1539918. B.J.R. and R.D.M. conceived of the experiment, E.D.B., N.J.G., and F.R. grew the samples, B.J.R. and R.D.M. performed the focused ion beam lithography, B.J.R., J.B.B., A.M., F.B., and R.D.M. designed and built the experiment, B.J.R., K.A.M., P.J.W.M., M.B., M.K.C., J.B.B., and R.D.M. performed the experiment, B.J.R. and K.A.M. analyzed the data, Y.Z. and E.A.K. developed the tight-binding model and provided theoretical guidance, and B.J.R. wrote the manuscript with input from all coauthors.

SUPPLEMENTARY MATERIALS

We used focused ion beam (FIB) lithography to prepare single crystal samples of TaAs for high field transport measurements. This allows for careful control over the electrical contact geometry to avoid the effects of inhomogeneous current jetting (see section I). FIB also allows for the production of samples with high geometric aspect ratios, enhancing the resistance to obtain sufficiently large signals for the pulsed field environment. We discuss the effects of surface degradation due to the FIB process.

As noted in the main text, ρ_{zz} appears to be activated in temperature above 50 tesla: we fit the conductivity to a simple model to extract a background plus a gap that increases with magnetic field (section II). A normalization procedure was applied to the conductivity: we show that this does not affect the extraction of the gap parameter.

In addition to the u -shaped sample shown in the main text two other ρ_{zz} samples were fashioned that show the gap opening above 50 tesla (section III). One sample had the field applied 35° from the \hat{c} -axis and shows all features scaling roughly as $1/\cos(\theta)$, as expected [37].

A brief analysis of the quantum oscillations was performed in section IV to estimate the quasiparticle lifetime and to show consistency with the more complete Fermi surface analysis by Arnold et al. [29].

Further information about the pulse-echo ultrasound technique employed here is described in section V, as well as full a data set of the sound velocity from 0 to 65 tesla.

The numerical diagonalization of the tight binding model for TaAs is shown in section VI, including a discussion of the Zeeman effect.

I. SAMPLE PREPARATION

Negative magnetoresistance has been reported for a large number of candidate Dirac and Weyl semimetals [16]. The observation of decreasing resistance with increasing magnetic field for $J||B$ has been taken as evidence of the chiral anomaly. Some of these measurements have been disputed because of extraneous effects that can also lead to an apparent negative mag-

netoresistance. In particular for TaAs, the highly anisotropic nature of the magnetoresistance means that current injected into the sample through point-like contacts does not necessarily move uniformly through the sample. This effect has been known for quite some time (see page 43 of Pippard [33]), and recent numerical simulations explored this in the context of Weyl semimetals by dos Reis et al. [34]. The result is that the potential drop across a pair of voltage contacts may not reflect the total current injected into the sample, depending on where the contacts are placed. This can be overcome by avoiding point-like contacts and by preparing samples with high aspect ratios with current injection taking place far from the voltage measurement. Even a standard precaution such as contacting the entire ends of a sample to inject current homogeneously does not necessarily produce consistent results since microscopic contact to the sample can still be point like or at the very least inhomogeneous.

To illustrate this point for TaAs we prepared the sample shown in Figure S1. The current path is highlighted in purple; the ‘good’ voltage contacts in red; the ‘bad’ voltage contacts in green. The corresponding resistances, or rather the voltage drop across the contacts divided by the nominal current, are shown in the two right hand panels for $B \parallel J \parallel \hat{c}$: the top panel corresponds to the green-shaded contacts offset from the current path; the bottom panel corresponds to the red-shaded contacts that are closer to the current path. It is immediately clear that a sizable “negative magnetoresistance” is visible for the green contacts at all temperatures, similar in character to that reported as evidence for a chiral anomaly in TaAs by Zhang *et al.* [30] and Huang *et al.* [23]. In our exaggerated geometry the voltage drops to near-zero at high fields: clearly an unphysical result. The apparent increase in this effect at higher temperatures is due to the increase in resistance and decrease in resistive anisotropy at higher temperatures: it takes more magnetic field to isolate the current from the green voltage contacts at higher temperatures because the resistive anisotropy is lower. The red contacts, on the other hand, show positive magnetoresistance that saturates at approximately 1 tesla—this is expected as $\omega_c \tau$ reaches 1 near this field value. We used an even more restricted current path geometry for the data presented in the main text, and a second sample with similar current path characteristics shows similar resistivity in Figure III.

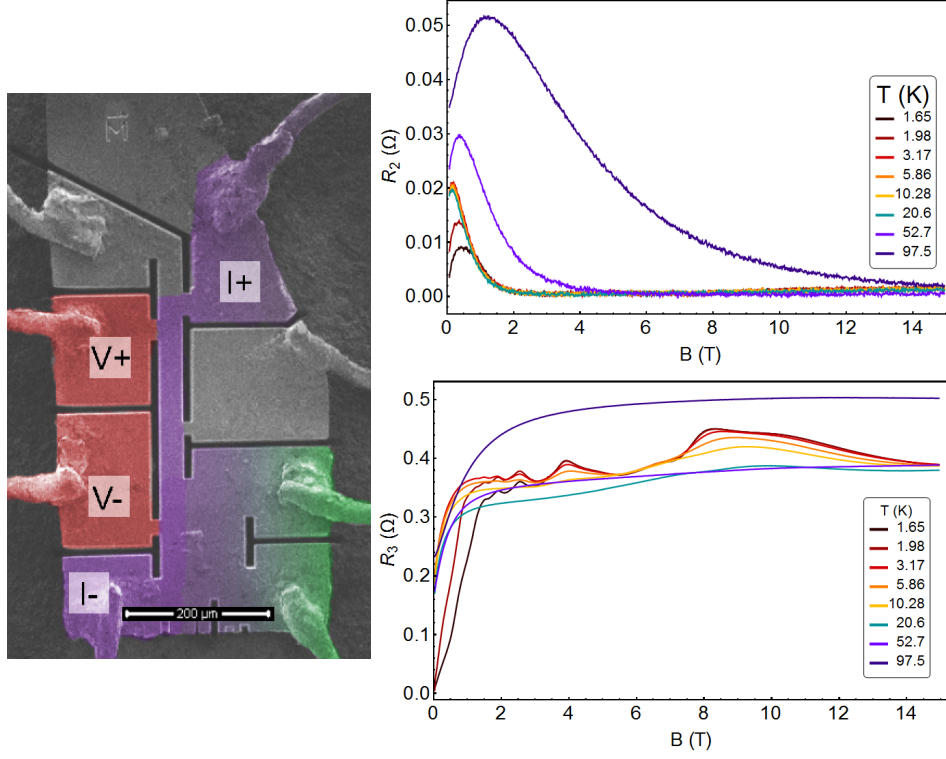


FIG. S1. **Demonstration of geometry-induced negative magnetoresistance in TaAs.** *Left:* Single crystal TaAs prepared through focused ion beam lithography to demonstrate the effects of inhomogeneous current paths. The current is injected along the purple path: the voltage is measured at the red contacts—near the current path—and at the green contacts—away from the current path. The crystalline \hat{c} -axis points along the current path: we applied B along this direction as well. *Upper right:* Apparent resistance measured at the contact pads shaded in green. A large negative magnetoresistance is observed at low fields: at high fields no voltage drop is observable due to the fact that no current travels near the green contacts. *Bottom right:* Contact pads placed along the current path reveal the “intrinsic” resistance of the material: roughly constant background magnetoresistance with quantum oscillations above 1 tesla, where $\omega_c\tau \approx 1$.

ρ_{zz} shown in Figure 1 of the main text show signs of saturation at the highest resistance values. This may be due to a parallel conduction channel on the surface of the sample. There are two possible sources of this conduction channel: the surface states which are known to be

present on this material and which have been observed via ARPES [9]; and/or an amorphous arsenic-depleted layer induced by the FIB [26].

As can be clearly seen in the inset of Figure 1 in the main text, the FIB prepared samples undergo a superconducting transition at low temperatures and low magnetic field. This is also a surface effect: it was recently shown that after FIB microstructuring the related material NbAs develops an amorphous arsenic-depleted surface layer, as arsenic is preferentially removed during the FIB process, leaving behind a niobium (or in our case tantalum) rich layer that is superconducting [26]. This superconductivity is fully suppressed above 2 tesla and 1.5 kelvin, and thus does not affect the majority of the data presented.

While the presence of a conducting surface layer changes the shapes of our resistivity curves at high fields, it does not alter any of the features from which we draw our main conclusions: the positions of the quantum limits for the various pockets, the onset of the resistivity increase in ρ_{zz} near 50 tesla, the temperature dependence of the increase in ρ_{zz} , the lack of a strong increase near 50 tesla in ρ_{xx} , and the sharp downturn in ρ_{xx} near 80 T below 4 K. The consistency of the ultrasound with the features in the transport provides further confirmation of the intrinsic nature of these features, as there was no FIB lithography performed on the ultrasound sample.

II. ACTIVATION FITS TO THE CONDUCTIVITY

We fit the conductivity $\sigma_{zz}(= 1/\rho_{zz})$ at each field slice as a function of temperature to a simple model: a background σ_b plus an activated component

$$\sigma_{zz} = \sigma_b + \sigma_0 e^{-\alpha/T}, \quad (2)$$

where α is the gap in units of kelvin. These fits plus the field-dependent fit parameters are shown in Figure S2.

In order to fit the gap down to the lowest possible field we normalized the conductivity to its value at 47 tesla. Figure S2 demonstrates that while this procedure changes σ_b and σ_0 it leaves Δ relatively unchanged. This is because the exponential factor dominates the fit, producing variability in σ_b and σ_0 that depend on how (which field value, for example) the normalization is

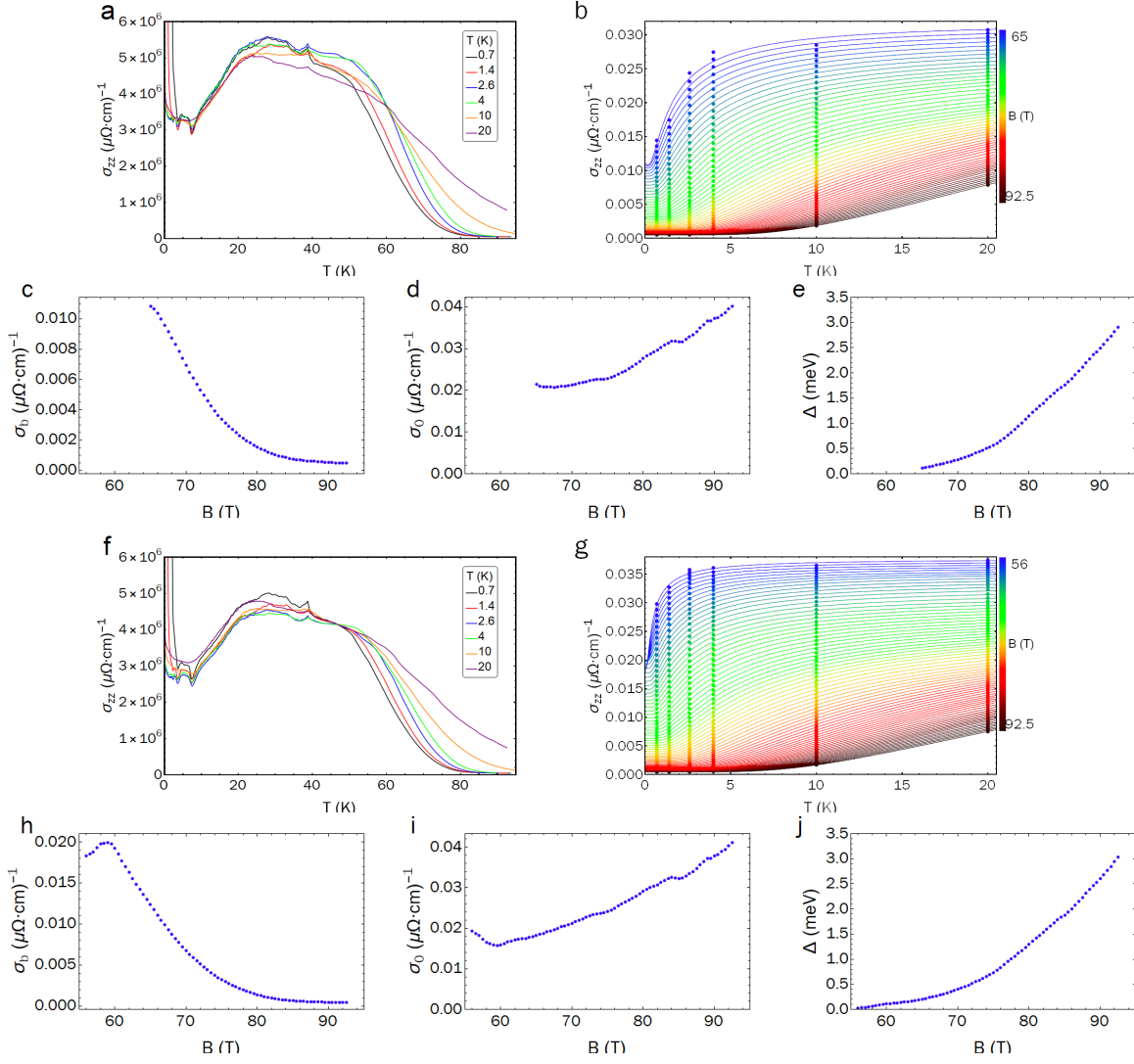


FIG. S2. **Fits to σ_{zz} as a function of temperature for different magnetic field values.** **a**, Raw conductivity data: the feature near 40 tesla is a voltage spike induced when the capacitor bank is discharged into the insert magnet. **b**, The conductivity in **a** is fit to $\sigma_{zz} = \sigma_0 + \sigma_1 e^{-\frac{\Delta}{k_B T}}$, with fit parameters shown in **c**, **d**, and **e**. Fits below 65 T are impossible due to a temperature-dependent background. To alleviate this we normalized the conductivity to the 20 kelvin value at 47 tesla (**f**), with the resultant fit shown in **g** and parameters in **h**, **i**, and **j**. Note that Δ is largely independent of this procedure.

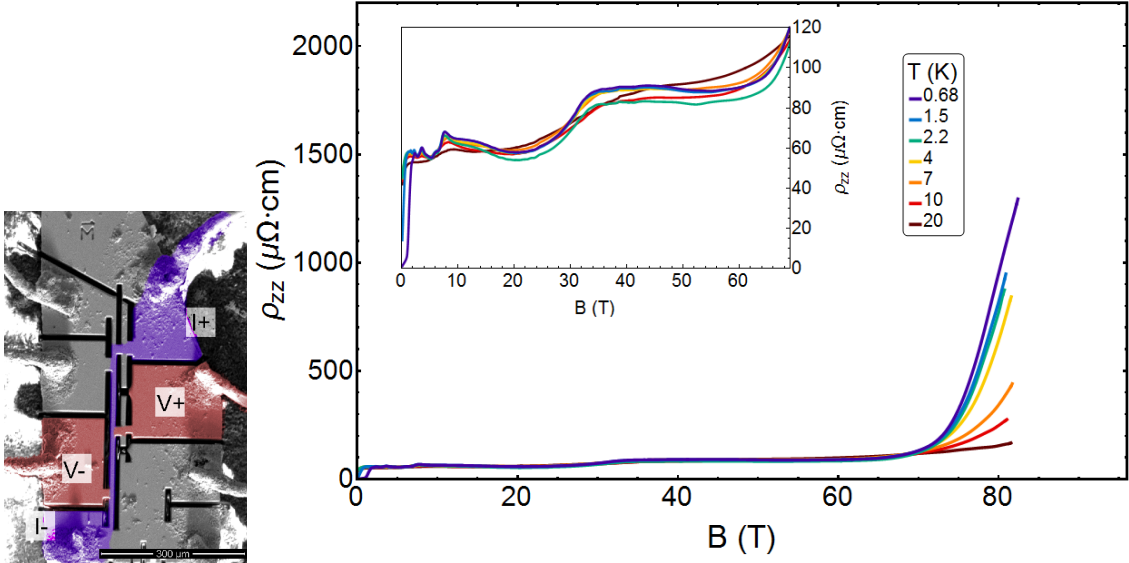


FIG. S3. $J||B$ resistivity for TaAs sample number 2. *Left*: the same sample shown in Figure S1 but with the current path (purple) restricted further, and voltage was measured between the red contacts. *Right*: Resistivity up to 82 tesla from 0.68 to 20 kelvin. Most features are qualitatively similar to those in Figure 1 of the main text, barring a more pronounced feature at the ultra-quantum limit of the hole pocket near 36 tesla.

carried out but leaving Δ procedure-independent. While σ_0 is a physical parameter representing background conductivity in TaAs, the extracted values of σ_b and σ_0 should not be taken as intrinsic.

III. REPRODUCIBILITY ON OTHER TaAs SAMPLES

A second TaAs sample (sample 2) in the $\vec{J}||\vec{B}||\hat{c}$ geometry was constructed to reproduce high field features in ρ_{zz} . This sample, shown in Figure S3, is actually the same as shown in Figure S1 but with the current path even more restricted.

The ρ_{zz} data in Figure S3 is qualitatively similar to that shown in Figure 1 of the main text (sample 1): both show the quantum limit of Weyl pockets near 7.5 tesla, both have a nearly field and temperature independent resistivity beyond the ultra quantum limit of the hole pocket at 36

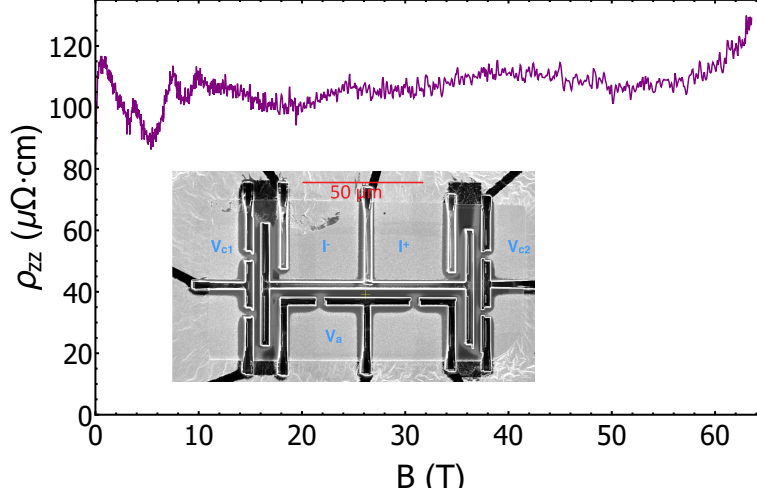


FIG. S4. \hat{c} -axis resistivity for TaAs sample number 3. This sample is prepared by plasma focused ion beam lithography (xenon rather than the gallium used for samples 1 and 2). Resistance curve is shown at 2.9 kelvin for B applied approximately 35 degrees off from the \hat{c} -axis. This offset has scaled all features by roughly $1/\cos(35^\circ)$.

tesla, and both show the onset of increased resistivity in the 50 to 60 tesla range (depending on temperature). The difference near the ultra-quantum limit could be due to different mobilities between sample 1 and sample 2, or due to a slight misalignment in the $\vec{J}||\vec{B}||\hat{c}$ geometry. Because the hole pocket has an aspect ratio of more than 10:1, a 15° offset can produce a large change in curvature factor (easily a factor of 3 for a mass anisotropy of 10 [51]) and hence a large change in oscillation amplitude from this pocket. Nevertheless the conductivity above the quantum limit, and before the gap opens above 50 tesla, is roughly field-independent.

Figure S4 shows a third sample prepared by plasma FIB, with the field applied approximately 35 degrees off from the \hat{c} -axis. This pushes the quantum limit of the Weyl pockets up to around 9.5 tesla from 7.5 tesla, the ultra-quantum limit of the hole pocket up to approximately 40 tesla from 36 tesla, and the onset of the gap to 60 tesla from 50 tesla. This increase in the onset field as the field is rotated toward the plane in which the Weyl nodes are separated was predicted by Kim et al. [37].

IV. QUANTUM OSCILLATIONS AND DINGLE FACTORS

According to the detailed quantum oscillation studies performed by Arnold et al. [29], TaAs contains three distinct types of Fermi surface: electron-like W1 Weyl surfaces, electron-like W2 Weyl surfaces, and hole-like trivial surfaces. We do not attempt to re-create their entire analysis here, but instead focus on the oscillations we observe in the $\vec{J}||\vec{B}||\hat{c}$ transport geometry. A complete treatment of the oscillation frequencies requires a full angle dependence which we have not measured: the purpose of the following analysis is to obtain a reasonable estimate for the quasiparticle lifetime τ for the Weyl electrons and to provide further evidence that the ≈ 18 T oscillation frequency is indeed coming from the same hole pocket identified by Arnold et al. [29].

The full \hat{c} -axis conductivity, including both background and oscillatory contributions, can be written at fixed angle as

$$\sigma_{zz} = \sum_i \sigma_0^i(B) \left(1 + \sum_p A^{i,p} R_T^{i,p} R_D^{i,p} \cos\left(2\pi p \frac{F_i}{B} + \phi_i\right) \right), \quad (3)$$

where the first sum is over the i distinct Fermi surfaces, the sum p is over the harmonics, $\sigma_0^i(B)$ are the field-dependent background conductivities, $A^{i,p}$ are amplitude factors, F_i are the oscillation frequencies (proportional to the Fermi surface cross sectional area), and ϕ_i are phase factors [51]. The temperature factor is given by

$$R_T^{i,p} = \frac{\frac{2\pi^2 p k_B T}{\hbar \omega_c^i}}{\sinh\left(\frac{2\pi^2 p k_B T}{\hbar \omega_c^i}\right)}, \quad (4)$$

where $\omega_c^i = eB/m_i^*$ is the cyclotron frequency for effective mass m_i^* . The Dingle factor is

$$R_D^{i,p} = e^{-\frac{\pi p}{\omega_c^i \tau_i}}, \quad (5)$$

where τ_i is the quasiparticle lifetime.

It is important to note that the background conductivities in Equation 3 are multiplicative with the oscillation amplitudes, not additive. Thus if a piece of Fermi surface does not contribute to σ_{zz} then its oscillations will not be visible in ρ_{zz} , even if the quasiparticle lifetime for that

surface is long. The W1 pockets are roughly elongated ellipses (see Figure 3C of Arnold et al. [29]) with an aspect ratio of approximately 10:1 with the long axis oriented along the \hat{c} direction. With an in-plane Fermi velocity of 3×10^5 m/s these surfaces dominate the ρ_{xx} transport and produce strong Shubnikov-de Haas oscillations with $B||\hat{c}$. For the ρ_{zz} transport, however, we expect their Fermi velocity along \hat{c} to be reduced by the aspect ratio (a factor of 10, so $v_z \approx 3 \times 10^4$ m/s), and thus contribute very little to the ρ_{zz} transport. The W2 Weyl surfaces, on the other hand, are roughly isotropic in aspect ratio and have $v_z \approx 1.6 \times 10^5$ m/s; the hole pocket has $v_z \approx 7 \times 10^5$ m/s. As conductivity is proportional to Fermi velocity squared, ρ_{zz} should be dominated by the W2 electron and trivial hole pockets. Note that the oscillations from a particular pocket can still be small due to other factors: for example, the hole pockets for $B||\hat{c}$ have a very unfavourable curvature factor that reduces their oscillation amplitude considerably (oscillation amplitudes scale as $1/\sqrt{\partial^2 A/\partial \kappa^2}$, where A is the extremal area of the Fermi surface perpendicular to the magnetic field and κ is the momentum direction parallel to the magnetic field) [51].

We forgo the usual Fourier analysis of our data which can be difficult when there are only a few oscillations [52]. We instead perform a full three-dimensional fit to Equation 3 for our data at temperatures where superconductivity is suppressed ($T = 2.6, 4, 10$ and 20 K). We can account for most features in the data fitting with $F_{W2} = 6.5$ T, $F_H = 17.2$ T, $m_{W2}^* = 0.1 m_e$, $m_H^* = 0.2 m_e$, $\tau_{W2} = 0.6$ ps, and $\tau_H = 0.4$ ps (see Figure S5). Values of $F_{W2} = 5.5$ T and $m_{W2}^* = 0.105 m_e$ were obtained by Arnold et al. [29] for the W2 Weyl pocket measuring magnetic torque with field along the \hat{a} direction: given the relatively isotropic nature of this pocket we believe that we are observing the same piece of Fermi surface. Values of $F_H = 18.8$ T, and $\tau_H = 0.11$ ps were obtained for the hole pocket by Arnold et al. [29], which again are in reasonable agreement with our own. Note that Arnold et al. [29] were unable to obtain a mass for the hole pocket for $B||\hat{c}$ but predicted a mass of $m_H^* = 0.17 m_e$ —very close to our experimentally determined $m_H^* = 0.2 m_e$ for this pocket.

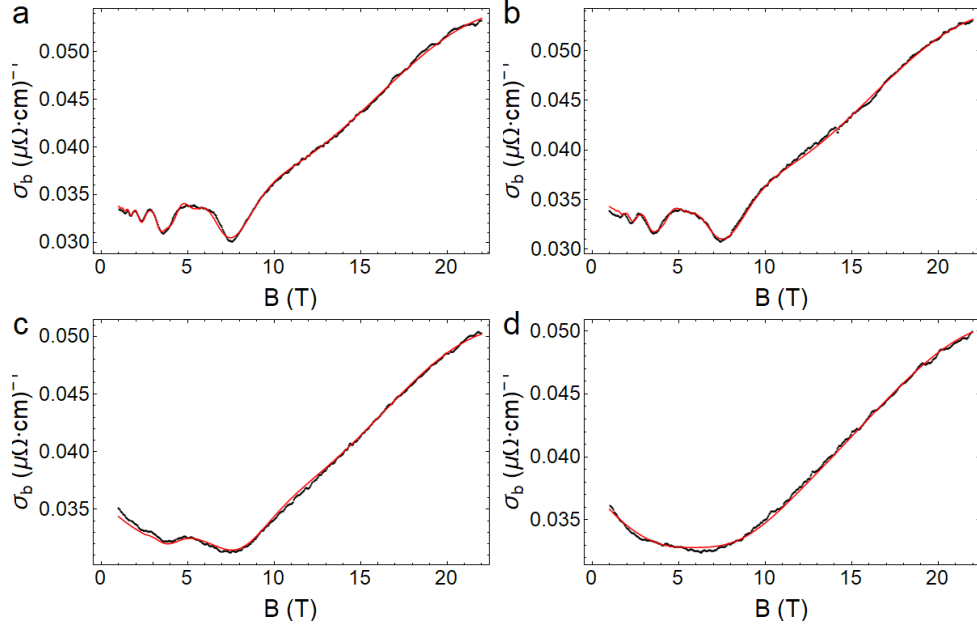


FIG. S5. **Fits to the oscillatory conductivity.** The conductivity for the sample discussed in the main text at 2.6 (a), 4 (b), 10 (c), and 20 (d) kelvin. Data is in black, fits to Equation 3 are in red. A third order polynomial in temperature and field is used to fit the background.

V. PULSE ECHO ULTRASOUND

Pulse echo ultrasound measures the speed of sound v transmitted through a sample for a specified sound propagation direction and polarization. Elastic moduli can then be computed via the relation $v = \sqrt{\frac{c}{\rho}}$, although care must be taken when choosing the propagation and polarization directions if the relationship between v and any particular c_{ij} is to be kept simple (see Brugger *et al.* [53]). The measurement typically involves generating a short burst of ultrasound (of order a few hundred nanoseconds) via a piezoelectric transducer, and then recording the echoes with the same transducer as the sound travels back and forth between the faces of the sample parallel to the transducer face. The phase shift between each successive echo is related to the travel time (and hence sound velocity) of the sound pulse, and the amplitude decay with successive echoes is related to the ultrasonic attenuation.

Our implementation of pulse echo ultrasound was similar to Suslov *et al.* [54] with one no-

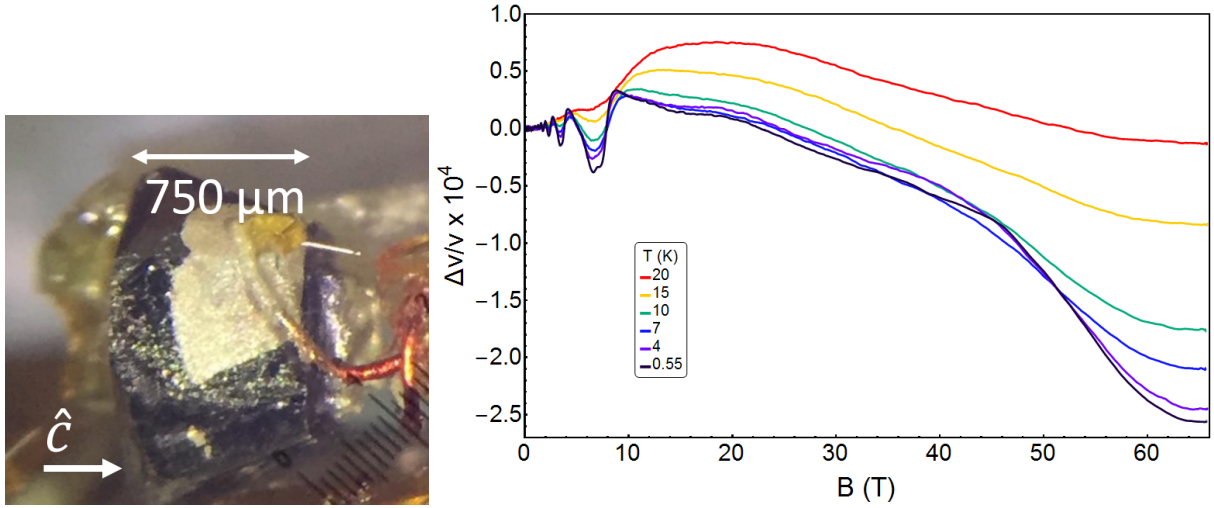


FIG. S6. **TaAs sample and ultrasound data from 0 to 65 tesla.** *Left:* TaAs sample used for ultrasound. Two parallel faces approximately $500 \times 500 \mu\text{m}^2$ were polished perpendicular to the \hat{c} axis. The sample was grounded with silver paint since the backside of the LiNbO₃ transducer was inaccessible. *Right:* Change in sound velocity from 0.55 to 20 K, from 0 to 65 tesla.

table exception: we forwent the mixing stage and directly recorded the full ultrasonic waveform with a 6 GS/s digitizer card (GaGe EON Express). This has two major advantages: it eliminates a large fraction of the electronics; and it allows the use of digital filtering and lock-in techniques that can be optimized and re-processed after the experiment is completed.

We generated 315 MHz longitudinal ultrasound with a 36° Y-cut LiNbO₃ transducer affixed to a (0, 0, 1) face of a TaAs sample (Figure S6). As both the direction of propagation and the polarization are along \hat{c} , we probe purely the c_{33} elastic modulus in this tetragonal crystal [53]. The full field dependence at selected temperatures between 0.55 and 20 kelvin is shown in Figure S6. The velocity v is calculated from the phase shift ϕ between successive echoes as

$$\Delta v = -2\pi fl \frac{\Delta\phi}{\phi^2}, \quad (6)$$

where f is the ultrasonic frequency and l is twice the sample length. The absolute phase ϕ can be obtained from the absolute spacing between successive echoes (a less accurate measure of the sound velocity, but the only way to get the absolute value) via $v = 2\pi fl/\phi$. All plotted

velocity shifts are normalized to the phase shift at $B = 0$: the absolute shift as a function of temperature was not obtained.

VI. TIGHT-BINDING MODEL FOR TAAS

The primitive unit cell of TaAs consists of four sublattices, two Ta atoms and two As atoms, per primitive unit cell. The lattice structure has two mirror symmetries M_x and M_y , TRS, and is invariant under C_4 rotation followed by a translation along the \hat{z} axis. We consider a three-dimensional tight-binding model representing the TaAs lattice structure. Specifically, we consider one spinful orbital per lattice site, giving rise to eight bands in total.

Our tight binding model:

$$\begin{aligned}
 H = & t \sum_{\langle ij \rangle, s} c_{is}^\dagger c_{js} + \sum_i \Delta_i c_i^\dagger c_i \\
 & + i\lambda \sum_{\langle\langle ik \rangle\rangle, s, s'} c_{is}^\dagger c_{ks'} \sum_j [\hat{d}_{ijk} \cdot \vec{\sigma}_{ss'}]
 \end{aligned} \tag{7}$$

where t is the nearest neighbor hopping; Δ is a staggered potential: $\Delta_i = \pm\Delta$ depending on whether the lattice site contains Ta or As; λ is the amplitude of the spin orbit interaction between the next nearest neighbors; $s = \uparrow, \downarrow$ is the spin; and σ 's are the corresponding Pauli matrices. \hat{d}_{ijk} is the unit vector in the direction of $\vec{d}_{ij} \times \vec{d}_{jk}$, where j is an intermediate site between i and k . This Hamiltonian preserves time reversal symmetry.

A. Weyl semimetal symmetries and the number of Weyl points

TaAs has 24 Weyl points, of which 8 are in the $k_z = 0$ plane (W1) and the rest 16 (W2) are at finite k_z [7]. The 8-fold (16-fold) multiplicity of the W1 (W2) Weyl points are guaranteed by model symmetries (lattice and TRS). More generally, the total number of Weyl points has to be $8n_1 + 16n_2$, where n_1 and n_2 are the numbers of sets of W1 and W2 Weyl points, respectively. For example, we will show the minimal tight-binding model can give 8 Weyl points, while adding extra terms and anisotropy reproduces the 24 Weyl points.

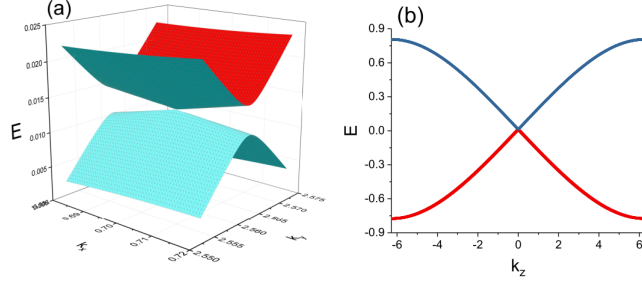


FIG. S7. The dispersion of the tight binding model in Eq. 7 in the (a) $k_x - k_y$ plane and (b) k_z direction around $\vec{k} = (0.7, 2.56, 0)$ shows that the gap closes at a single Weyl node and the nearby dispersion is linear. The model parameters are $t = 1.0$, $\Delta = 0.7$, and $\lambda = 0.1$.

A finite Δ in Eq. 7 explicitly breaks inversion symmetry, thus is vital to the emergence of Weyl semimetals. On the other hand, in the limit of $\Delta \rightarrow \infty$ the system has to be a trivial insulator. In the presence of TRS, a Weyl semimetal is guaranteed to exist between a topological insulator and a trivial insulator[55]. During the evolution, pairs of Weyl points are generated, transported across the momentum space, and re-annihilate in different pairs, giving rise to a change of the \mathbf{Z}_2 topological index. We note that the W2 Weyl points always change the topological index trivially by 2, and it is up to the W1 Weyl points to change the \mathbf{Z}_2 topological index by a nontrivial 1. This suggests that while the W1 Weyl points are essential and guaranteed to occur somewhere during the interpolation, the W2 Weyl points are less fundamental and involve more fine-tuning.

B. Results

First, we show that the Hamiltonian in Eq. 7 can give a Weyl semimetal in certain parameter regions. For model parameters $t = 1.0$, $\Delta = 0.7$, and $\lambda = 0.1$, the dispersion around $\vec{k} = (0.7, 2.56, 0)$ is shown in Fig. S7. The band touching at a single Weyl point and the nearby linear dispersion are clearly established. The locations of all the eight Weyl points within the momentum space are illustrated in Fig. S8. Being at $k_z = 0$, these Weyl points belong to the W1 group. Interestingly, we observe the shift and annihilation of the Weyl nodes as we change

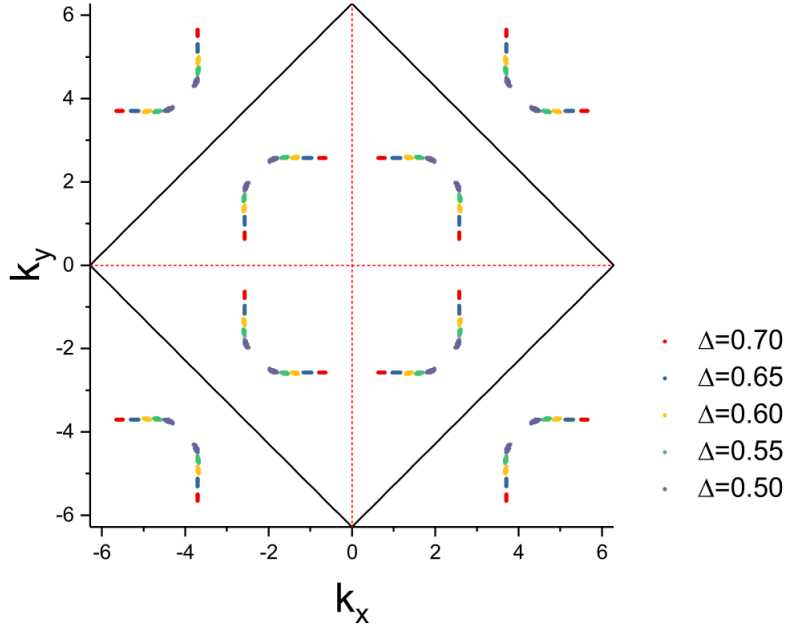


FIG. S8. The locations of the eight Weyl points in the $k_x - k_y$ plane at $k_z = 0$. The data points reflect the regions where the band gap falls below $0.03t$. The solid black lines mark the boundary of the Brillouin zone and the red dashed lines are the mirror symmetry planes. As Δ increases, the eight Weyl points approach each other and finally annihilate in pairs on the mirror planes at $\Delta \sim 0.8$, leading to a trivial insulator. Other parameters are $t = 1.0$, $\delta = 0.7$ and $\lambda = 0.1$.

the amplitude Δ of inversion symmetry breaking. We also note that the dispersion between the pair of adjacent Weyl nodes resembles that observed in band-structure calculations[25].

A parallel comparison between the electronic structure of the minimum tight-binding model and that of the actual TaAs crystal from band-structure calculation from Ref. [23] are included in Fig. S10. The minimum model in Eq. 7 is already capable of qualitatively resembling the ab-initio band structures near the chemical potential.

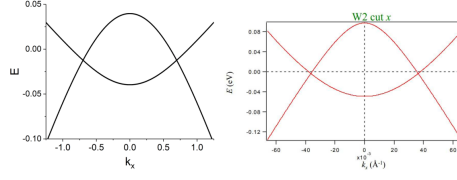


FIG. S9. The dispersion along the pair of adjacent Weyl nodes. Left: tight-binding model with parameters $t = 1.0$, $\delta = 0.7$ and $\lambda = 0.1$ for illustration; right: DFT calculation results from Ref. [25] along a cut through the W2 Weyl nodes.

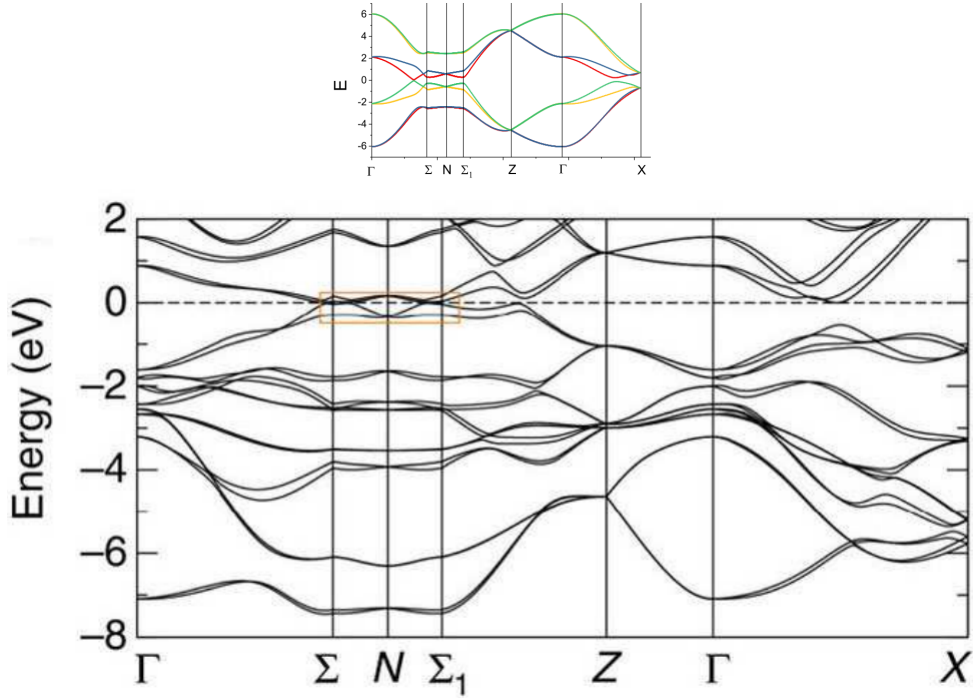


FIG. S10. The bulk electronic structure of (upper) the tight-binding model in Eq. 7 and (lower) DFT band-structure calculations from Ref. [23]. The tight-binding model parameters are $t = 1.0$, $\Delta = 0.7$, and $\lambda = 0.1$.

VII. CONSEQUENCES OF A MAGNETIC FIELD

We now consider the fate of the Weyl physics in the presence of an external magnetic field. For simplicity, we first focus on the situation when the magnetic field is along the c axis: $\vec{B} =$

$B_z \hat{z}$. Since k_z remains a good quantum number, together with the quantization within the $k_x - k_y$ plane, gives rise to Landau bands. For an individual Weyl node, there exists a chiral Landau band, whose up-moving or down-moving is associated with the chirality of the original Weyl node. However, as discussed in other theoretical studies, this physics becomes challenged at large magnetic fields[37, 38].

A. Anti-crossing of the chiral Landau levels

Semi-classically, magnetic fields introduce finite resolution in $k_x - k_y$ momentum space, inversely proportional to the magnetic length. Therefore, at large enough B , the pair of separated Weyl nodes with opposite chirality becomes indistinguishable and magnetic breakdown makes tunneling between them non-negligible. This was addressed schematically in Ref. [37, 38]. Here, we will study from the perspective of our tight-binding model in Eq. 7. We find an emergent gap whose amplitude and onset field are roughly consistent with those observed in experiments for Weyl node separation $\delta k \sim 0.15\pi/a$, which is at least a factor of 2 larger than DFT results[23, 25] yet can be attributed to a relatively small modification to the overall band structure. Since the separation between the pair of adjacent Weyl fermions are small, they are very sensitive to small shifts in bandstructure which may be beyond the resolution capability of the DFT calculations. We also note that the Weyl nodes separation $\delta k \sim 0.15\pi/a$ is consistent with the position of the Weyl nodes in the surface Brillouin zone observed in ARPES experiments[27]. As most studies have found W2 Weyl fermions to have larger separations than the W1 Weyl fermions, the former should be more resilient and dominates the fate of the Weyl physics in large magnetic fields. Although the W2 Weyl nodes are away from the $k_z = 0$ plane, it only causes a constant shift to the zero of the k_z good quantum number and does not change the following discussion. The k -space distance between different pairs of Weyl nodes is much greater than the intra-pair separation and quantum tunneling due to magnetic breakdown between different pairs can be neglected.

In this subsection, we neglect the Zeeman effect, and the vector potential of the magnetic field is chosen as $\vec{A} = (0, Bx, 0)$. We also set Fermi velocities in the $v_F^x \sim v_F^y \sim$

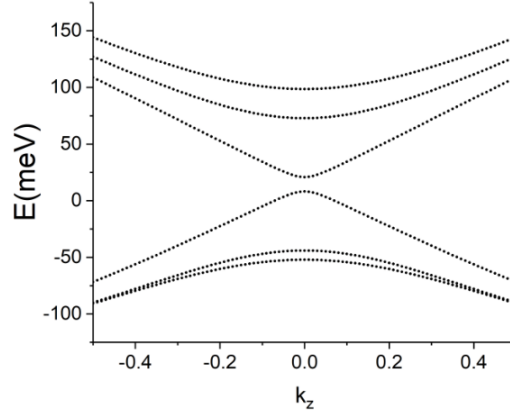


FIG. S11. Landau band dispersion along the k_z direction obtained for the tight-binding model in Eq. 7. $t = 1.0$, $\Delta = 0.7$, and $\lambda = 0.1$. The vector potential A applied is equivalent to the W2 Weyl nodes in the presence of a magnetic field $B_z = 145T$. Each band is four-fold degenerate. The bands at higher and lower energies are the non-chiral Landau bands at indices $n = \pm 1, \pm 2$.

$291,000m/s = 1.92eV \cdot \text{\AA}$ observed via quantum oscillation measurements. These, together with the Weyl node separation $\delta k \sim 0.15\pi/a$ and $a = 3.437\text{\AA}$ in TaAs allows us to set proper units for our numerical results.

A typical Landau band dispersion is illustrated in Fig. S11. Each band is four-fold degenerate, suggesting the tunneling between different pairs of Weyl nodes are still negligible even at a large magnetic field $B_z = 145T$. On the other hand, a gap is clearly observable between the $n = 0$ chiral Landau bands.

An important question is how does the size of this anti-crossing gap depends on the applied magnetic field. Intuitively, the gap should be exponentially suppressed at smaller field $l_B \delta k \gg 1$, and scale linearly at larger magnetic field. Such behavior is clearly observed in Fig. S12 and Fig. S13, where the units of the data are interpreted for TaAs W2 Weyl nodes with separation $\delta k = 0.15\pi/a$ and $\delta k = 0.165\pi/a$, respectively.

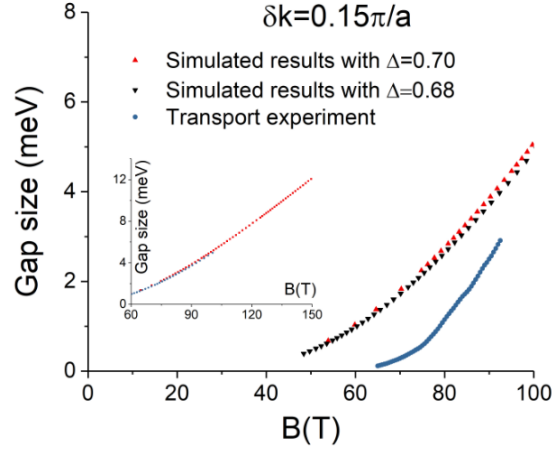


FIG. S12. The size of the gap between the $n = 0$ chiral Landau bands versus the magnetic field. Two numerical simulations are carried out with $\Delta = 0.68$ and $\Delta = 0.70$, respectively. $t = 1$ and $\lambda = 0.1$ for both. The low-energy physics around the pairs of Weyl nodes is compared with experimentally-measured properties for the W2 Weyl nodes in TaAs: $v_F^x \sim v_F^y \sim 1.92eV \cdot \text{\AA}$ and $\delta k \sim 0.15\pi/a$. The values of the gap extracted from the temperature dependence in transport experiments are also listed for comparison. Inset: at larger magnetic field the gap shows a linear dependence.

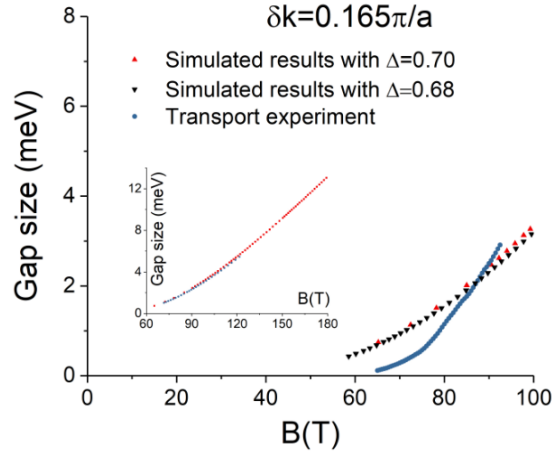


FIG. S13. Same as Fig. S12, except the separation between the Weyl nodes in TaAs is assumed to be $\delta k \sim 0.165\pi/a$. Note the sensitive dependence of the gap size on δk .

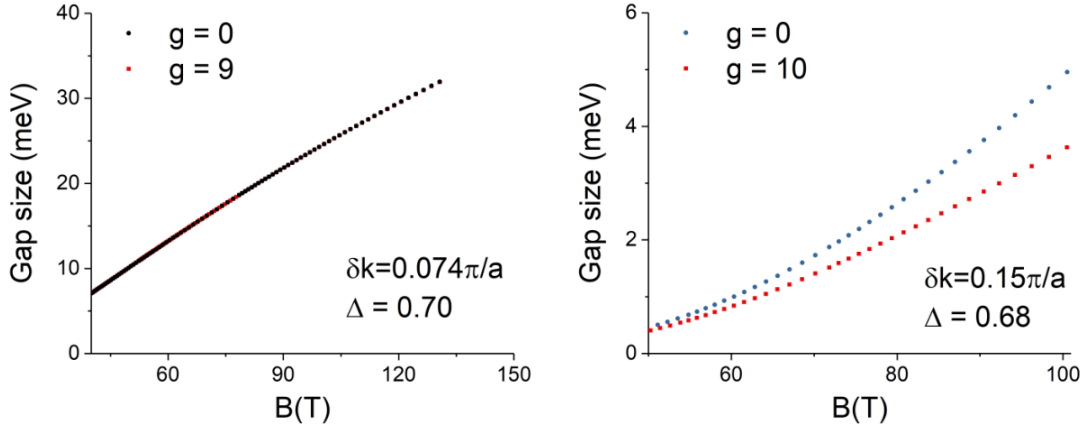


FIG. S14. Parallel comparisons of the magnetic field dependence of the gap opened between chiral Landau levels with and without the Zeeman effect incorporated as Eq. 8. Upper: $\Delta = 0.7$ in the tight-binding model and the data is interpreted for Weyl nodes separation $\delta k = 0.074\pi/a$; Lower: $\Delta = 0.68$ and $\delta k = 0.15\pi/a$ where smaller gaps make the Zeeman effect's impact more apparent. Both have $t = 1$ and $\lambda = 0.1$ as tight-binding mode parameters.

B. Impact of the Zeeman effect

Now we consider another potentially important ingredient—the Zeeman effect—particularly important because semi-metals and semi-conductors often give rise to large g -factors. To incorporate this we add an additional contribution to the Hamiltonian:

$$H_{\text{Zeeman}} = -\mu_B g S^z \quad (8)$$

The results with and without the Zeeman effect are compared in Fig. S14. The results suggest that though the impact of the Zeeman effect is relatively minor (Fig. S14 upper panel), the quantitative change to the anti-crossing feature is visible especially for larger Weyl nodes separation δk that allows weaker gaps with a larger magnetic field threshold, see Fig. S14 lower panel.

The influence of the Zeeman effect can be understood via its modifications to the band structure in the absence of the vector potentials, see Fig. S15. In the presence of Zeeman energy,

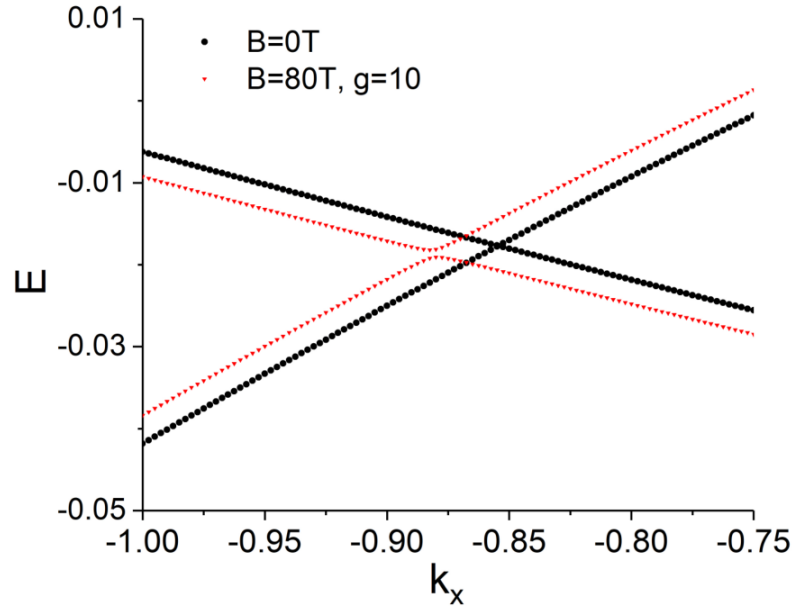


FIG. S15. The dispersion near a Weyl nodes along the direction to its pair counterpart without and with a Zeeman energy equivalent to 80T of magnetic field and a g -factor of 10. In the presence of the Zeeman energy, the Weyl nodes separation increases.

the Weyl nodes moves further apart, making quantum tunneling between the pair of Weyl nodes more difficult thus suppressing the anti-crossing gap size.